Lawrence Berkeley National Laboratory
Recent Work

Title

DESIGN AND CHARACTERIZATION FOR ABSOLUTE X-RAY SPECTROMETRY IN THE 100-10 000 eV REGION

Permalink

https://escholarship.org/uc/item/8h35g33z

Author

Henke, B.L.

Publication Date

1986-08-01

Lawrence Berkeley Laboratory

UNIVERSITY OF CALIFORNIA
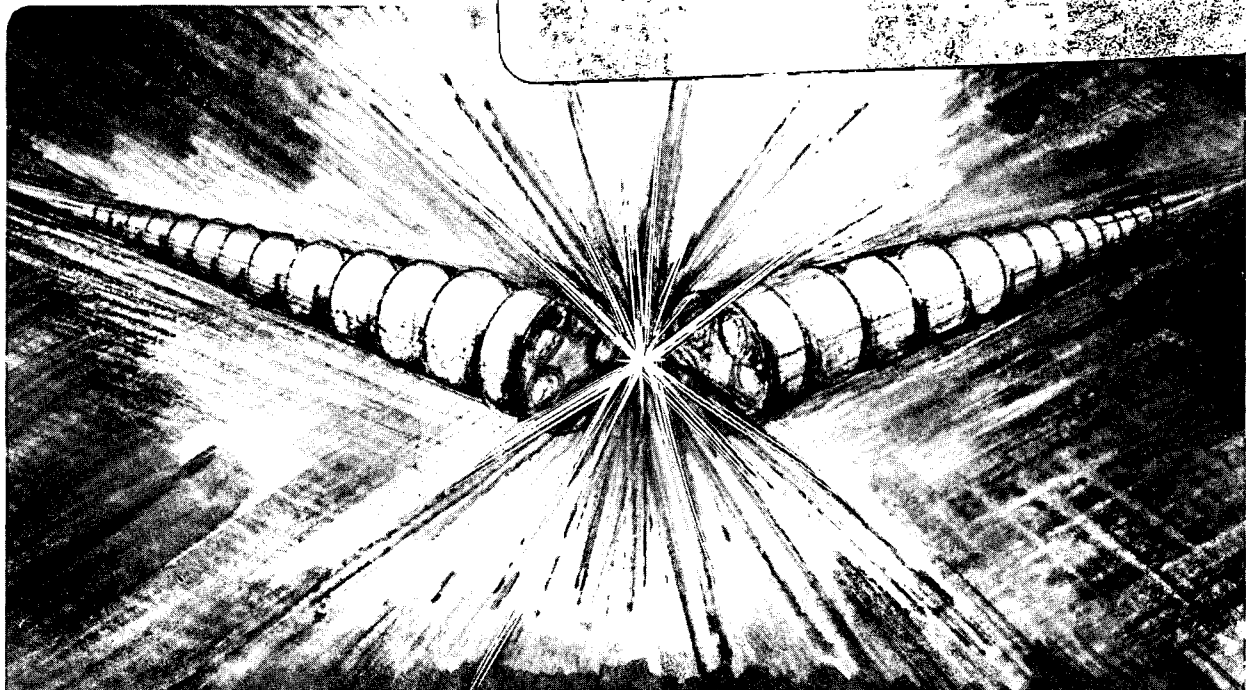
Accelerator & Fusion Research Division

Presented at the 11th International Congress on X-ray Optics and Microanalysis, London, Ontario, August 4, 1986

DESIGN AND CHARACTERIZATION FOR ABSOLUTE X-RAY SPECTROMETRY IN THE 100-10 000 eV REGION

B.L. Henke

August 1986

DISCLAIMER

DESIGN AND CHARACTERIZATION FOR ABSOLUTE X-RAY

SPECTROMETRY IN THE 100-10 000 eV REGION

A Review Prepared for Presentation at the
11th International Congress on X-Ray Optics and Microanalysis
University of Western Ontario
August 4, 1986

Burton L. Henke
Center for X-Ray Optics
University of California
Lawrence Berkeley Laboratory
1 Cyclotron Road
Berkeley, California 94720

ABSTRACT

Reviewed here are the design and characterization procedures used
in our program for developing absolute x-ray spectrometry in the
100-10 000 eV region. Described are the selection and experimental
calibration of the x-ray filters, mirror monochromators,
crystal/multilayer analyzers, and the photographic (time integrating)
and photoelectric (time resolving) position-sensitive detectors.
Analytical response functions have been derived that characterize the
energy dependence of the mirror and crystal/multilayer reflectivities
and of the photographic film and photocathode sensitivities. These
response functions permit rapid, small-computer reduction of the
experimental spectra to absolute spectra (measured in photons per
stearadian from the source for radiative transitions at indicated photon
energies). Our x-ray spectrographic systems are being applied to the
diagnostics of pulsed, high temperature plasma sources in laser fusion
and x-ray laser research.

I. INTRODUCTION

There is a considerable present need for the development of efficient absolute x-ray spectrometry for the characterization and application of the new high-intensity synchrotron and high-temperature plasma radiation sources. An example of a spectrographic system recently developed in this laboratory for time-integrated and time-resolved absolute spectrometry in the 100-10 000 eV region[1] is described in Fig. 1. Here the x radiation from a small source is line-imaged at a scatter aperture by reflection from an elliptically curved crystal/multilayer analyzer and then proceeds to form a normally incident spectrum along a detection
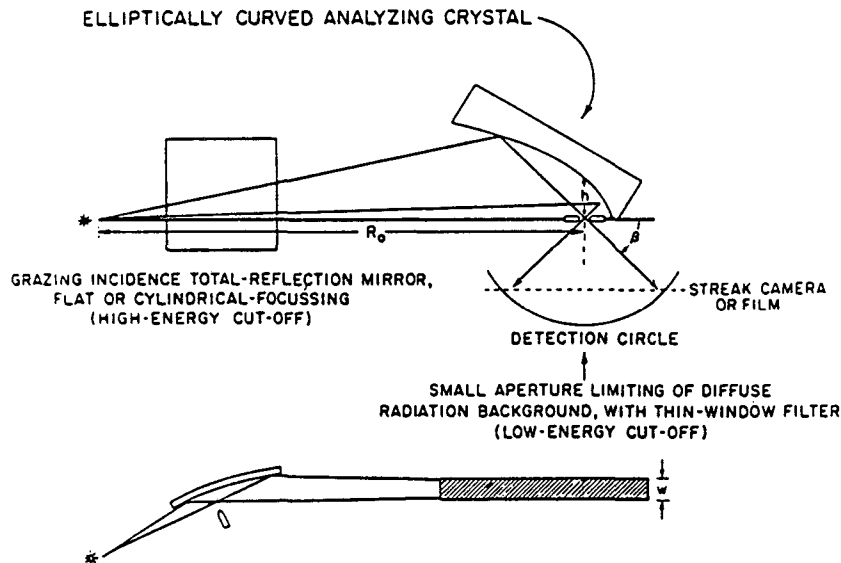
Fig. 1. The optical geometry of the elliptical analyzer x-ray spectrograph.

circle. The Bragg angle range of the spectrum presented by the elliptical analyzer is about 20-70°. The usually intense high and low energy x-ray background radiation from the synchrotron and plasma sources is effectively reduced by the band-pass characteristic of a primary monochromator combination of a mirror and filter. To obtain the required time-integrated and time-resolved absolute spectrometry, twin

channels are employed using both position-sensitive photographic film and streak camera detection (illustrated in Fig. 2). This instrument is now being applied in laser fusion and x-ray laser research using the
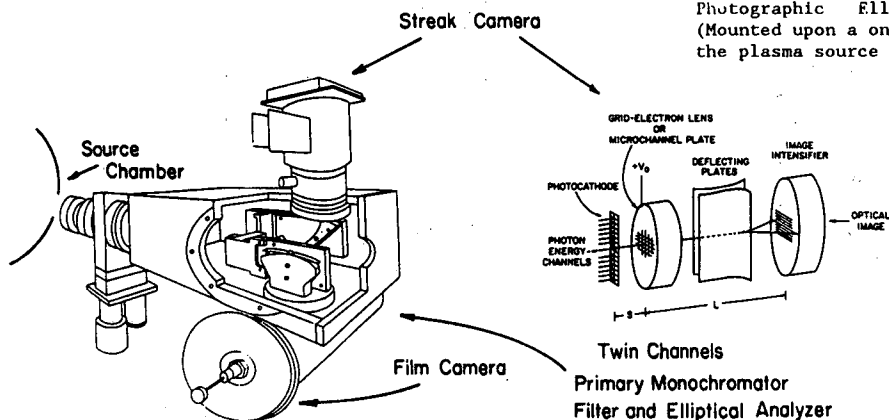
Fig. 2. The two-channel, SPEAXS system - Streak and Photographic Elliptical Analyzer X-Ray Spectrograph. (Mounted upon a one-meter target chamber with 120 cm between the plasma source and the scatter aperture.)

laser-produced plasma source of the OMEGA facility at the University of Rochester (utilizing 24 focussed UV laser beams of about 2000 joules total energy of 3510 A light within a 600 picosecond Gaussian pulse). Presented in Figs. 3 and 4 are examples of photographic and streak camera spectra obtained with this spectrograph on OMEGA.[2]

Fig. 3. Example of a photographically recorded spectrum with the SPEAXS system using the PET elliptical analyzer. Measured transitions are for the ionized species, Al^{11+}, Al^{12+}, Si^{12+} and Si^{13+} from a 200-μm-diameter glass microballoon coated with 1 μm of Al and excited by a 600-ps/200-J pulse of 351-nm light of the OMEGA facility. Exposure on RAR-2495 film.
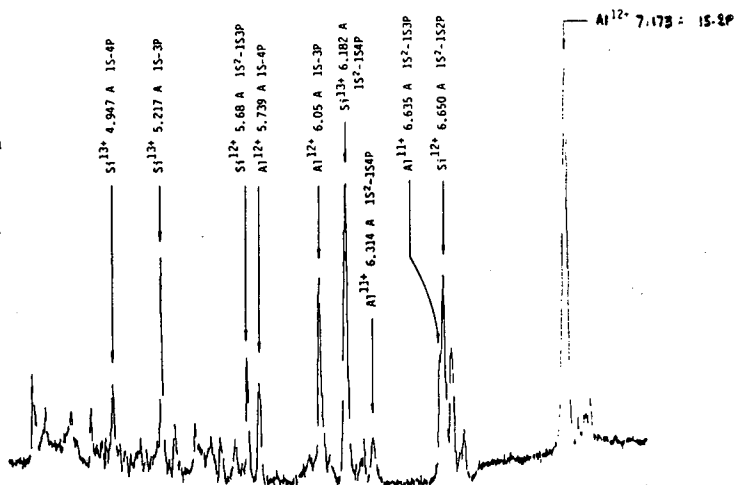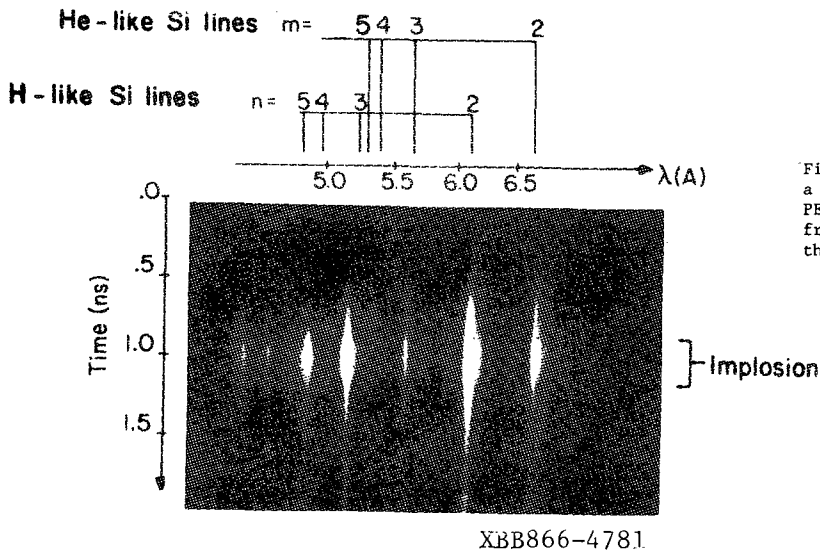
4

He-like Si lines m=   5 4 3   2

H-like Si lines   n= 5 4 3   2

XBB866-4781

Illustrated in Fig. 5 is the relationship between a spectral line
distribution of photons as measured at the detection circle and the
absolute intensity, i_0, of the source. It may be readily derived[3] that
i_0 is given by:

$$i_0 = N(L/FMR(d\chi/d\theta)) \qquad (1)$$

i_0 = PHOTONS/STRD
AT ENERGY, E
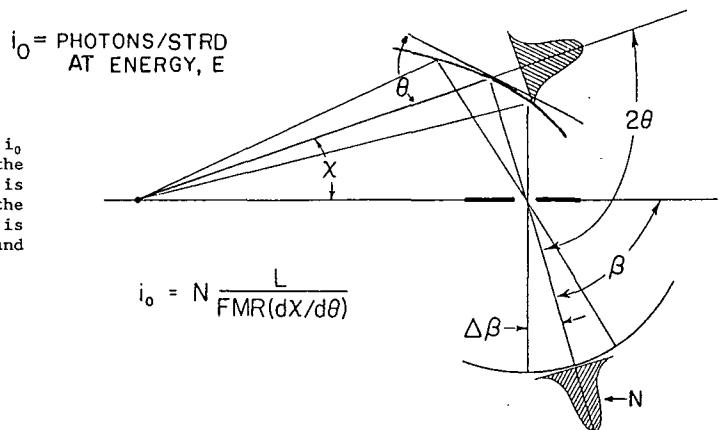
Fig. 5.   Relating the absolute source intensity, i_0
(photons/strd) to the total number of photons, N, within the
measured diffraction profile at the detection circle. F is
the filter transmission, M, the mirror reflectivity, R, the
crystal/multilayer integrated reflectivity, and $(d\chi/d\theta)$ is
the differential relation for the source emission angle and
the Bragg reflection angle.

$$i_0 = N \frac{L}{FMR(d\chi/d\theta)}$$

where:

i_0 = photons/stearadian emitted at the source for a given radiati e transition and at the measured photon energy of the spectral line;

N = the total number of photons measured within the spectral line distribution per unit length of the spectral line (in the direction normal to the plane of Fig. 5).

L = the constant total geometric length of any reflected ray from the source to the detection circle (this invariance is a characteristic of the elliptical focussing geometry);

F = filter transmission;

M = mirror reflectivity;

R = the integrated reflectivity characteristic of the crystal/ multilayer reflection measured in $\Delta\theta$ Bragg angle units; and

$d\chi/d\theta$ = the ratio of the differential angular width, $d\chi$, of the radiation from the source to the associated differential angular width, $d\theta$, of the radiation that is Bragg reflected from the analyzer.

Note: The response function (1) applies generally for any cylindrical analyzer geometry, since $d\chi/d\theta$ can be given as an analytical expression characteristic of the particular cylindrical analyzer geometry that is generating the diffraction line profile, whether it be convex, concave (e.g. elliptical, as here) or flat.[3]

Efficient absolute x-ray spectrometry is achieved by applying the response relationships[1,3] to the measured spectrum (e.g. via a small computer associated with the spectrographic system) to immediately yield the absolute intensity spectrum of the source. The individual response functions for the primary mirror-filter monochromator, the crystal/ multilayer analyzer and for the position-sensitive detectors may be derived by fitting analytical energy-dependent model relations to calibrations measured at a few photon energies that are representative of the range of measurement.

In this paper we review our procedures for establishing the required absolute response functions and present typical results for applied x-ray spectroscopy in the 100-10,000 eV region. In the Bibliography are listed the recent reports of this laboratory (including those in preparation) which describe in detail these characterization procedures and which establish the co-authorship of students and research associates for each particular research effort.

II. SPECTROGRAPHIC RESPONSE CHARACTERIZATION

A. Crystals/Multilayers

For our crystal/multilayer characterizations we obtain absolute experimental spectra at several photon energies which include the small angle "total-reflection" region, the first order diffraction line and any higher orders that may be allowed. The measurement geometry is shown in Fig.6. A narrow beam of incident radiation of intensity, $I_0\cos\theta$, defined by a fine slit at a demountable x-ray tube window and by a razor blade placed near the analyzer, is reflected by the crystal/multilayer to a gas-flow proportional counter, where monochromatic characteristic line x radiation from the source is isolated by an appropriate filter and by pulse-height discrimination
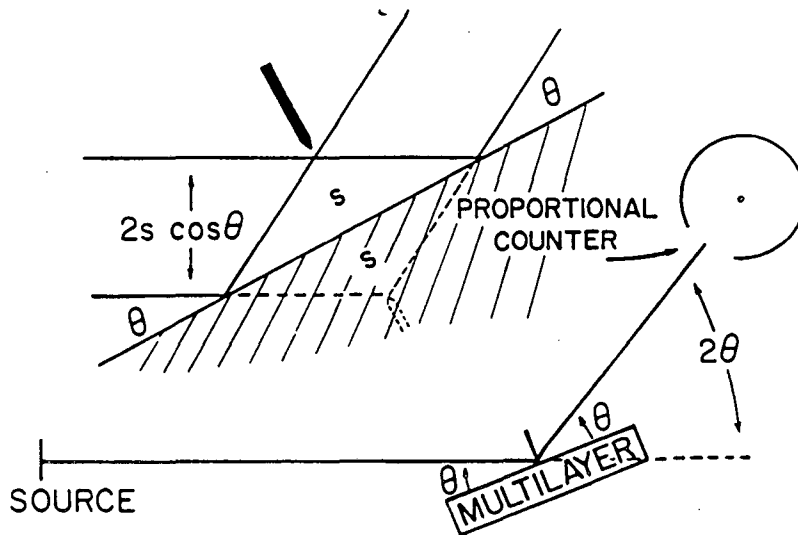
Fig. 6. Geometry for the measurement of crystal/multilayer reflectivity. The narrow incident x-ray beam intensity is $I_0 \cos \theta$ for reflection through the slit, while $I_0/2$ is the direct beam intensity that is measured at $\theta = 0$.

with the counter. (Any significant contamination background radiation will also appear in the measured spectrum and thereby the zero-angle incident beam can be corrected to yield the appropriate characteristic line intensity, $I_0/2$.)[4] The spectrum is step-scanned and appears first on a multichannel analyzer which permits reading out the critical angle for total reflection, θ_c, the integrated reflectivity, R, the

experimental FWHM, ω, and peak efficiency, P (defined in Fig. 7). As discussed in Ref. 4, the measured onset of the total reflection region signals an accurate goniometer zero-angle setting and the corresponding value of $I_0/2$. The critical angle for "total reflection," θ_c, can be used to yield an estimation of the analyzer's surface structure and refractive properties (optical constant, δ).
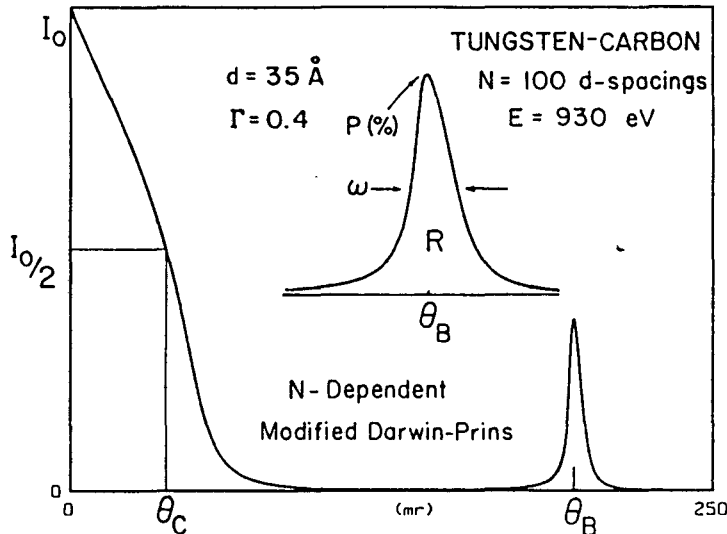

Fig. 7. Small-angle reflection and first order Bragg diffraction for a 100 layer tungsten-carbon multilayer. Tungsten thickness is 0.4 d (assumed sharp interfaces). Definition of the four experimental variables used to characterize the crystal/multilayer--the critical angle, θ_c, of reflection at $I_0/2$, the peak and integrated reflectivities, P and R, and the FWHM, ω.

We have recently developed a modification of the dynamical Darwin-Prins crystal reflectivity relation to extend its application for the low-energy x-ray region and for reflection by multilayer systems of a finite number of layers, N. Our analytical, modified Darwin-Prins model relation (MDP) can accurately predict the small-angle total reflection characteristic and all diffraction orders present for a given photon energy, and can allow the spectrum to be rapidly presented on a small computer screen and plotter (e.g. with the IBM PC equipped with a FORTRAN compiler). The derivation of this MDP analytical model is described in Refs. 4 and 5 and the resulting reflectivity equations are presented below.

As described in Fig. 8, the small fraction of the incident amplitude that is absorbed and reflected by a single layer of unit cells of the crystal, σ and s respectively, can be expressed in terms of the complex total scattering factor per unit cell, $F_0 (= F_{01} + iF_{02})$, and the structure factor of the unit cell, $F (= F_1 + iF_2)$. F_0 is equal to F at its forward-angle scattering limit (setting $\theta = 0$ in F). In the

Fig. 8. In the Darwin-Prins dynamical model for crystal reflection, the reflection ratio for the semi-infinite crystal, S_0/T_0, is determined by a summing of all possible multiply reflected and transmitted components at periodically spaced elementary layers of unit cells. Defined here are the small fractional amplitudes that are absorbed and reflected by a plane of unit cells, σ and s respectively, which are related to the structure factor, F, and scattering factor F_0 per unit cell. F_0 is given by the forward-scattering value of F.
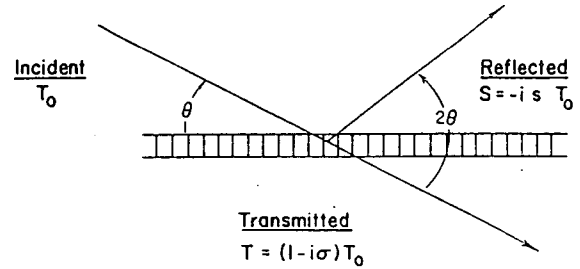
For $\underline{m}$ $\underline{Unit}$ $\underline{Cells}$/Unit Area of Structure Factor, $F_1 + iF_2$, and of Total Scattering Factor, $F_{01} + iF_{02}$, Per Unit Cell

$$\sigma = -mr_0\lambda \frac{F_{01} + iF_{02}}{\sin\theta} \quad \text{and} \quad s = -mr_0\lambda \frac{F_1 + iF_2}{\sin\theta} P(2\theta)$$

$P(2\theta) = 1$ or $\cos 2\theta$ for the Two Polarized Components

Darwin-Prins reflectivity model for an ideal, semi-infinite crystal (with reflecting planes parallel to the surface) the ratio of the total amplitude that is dynamically reflected, S_0, to that incident, T_0, is given by the expression:

$$S_0/T_0 = \frac{-y}{(1-z) \pm \sqrt{(1-z)^2 - y^2}} \qquad (2)$$

where

$$y = \frac{FP(2\theta)}{F_0} \qquad (3)$$

and

$$z = \frac{2\pi V}{r_0\lambda^2} \frac{\sin\theta \left[\sin\theta - (m\lambda/2d)\right]}{F_0} \qquad (4)$$

Here r_0 is the classical electron radius, λ the x-ray wavelength, d the unit cell thickness and crystal reflecting plane spacing, and V the unit cell volume. If the incident radiation is polarized (e.g. synchrotron

radiation) the appropriate value of S_0/T_0 is obtained by setting the polarization factor, $P(2\theta)$, equal to unity or $\cos 2\theta$ (σ or π component) and the corresponding intensity ratio for this polarized component, I/I_0, is obtained by multiplying S_0/T_0 given by (2) by its complex conjugate. (Note: The choice of plus or minus sign in this expression is that which yields a value for I/I_0 that is less than unity.) For unpolarized incident x-radiation, the reflected intensity ratio is given by one-half of the sum of the two polarized components (with $P(2\theta)$ equal to unity and $\cos 2\theta$ respectively).

In the definition of the parameter z, $m\lambda/2d$ equals $\sin \theta_0$, where θ_0 identifies an angular region for which S_0/T_0 has a significant value (i.e. for the small angle total reflection region $m = 0$, and for the first, second and third order diffractions, $m = 1,2,3...$, as given by the Bragg equation). In our computer program, this order parameter m, is automatically taken as the integer that is nearest the value of $2d \sin \theta/\lambda$, thereby permitting a continuous plotting of the spectrum throughout the entire range of reflection angles, θ.

In our modified Darwin-Prins model we multiply the expression for S_0/T_0 in (2) for the semi-infinite crystal by a factor which then yields the amplitude, S_{ON}/T_0, reflected from a multilayer of a finite number of layers, N, given by:

$$S_{ON}/T = (S_0/T_0) \frac{1-x^{2N}}{1 - (S_o/T_o)^2 x^{2N}} \qquad (5)$$

where

$$x = (-1)^m \exp(-\eta) \qquad (6)$$

and

$$\eta = \pm \frac{r_o \lambda d\, F_o}{V \sin\theta} \sqrt{y^2-(1-z)^2} \qquad (7)$$

(The plus or minus sign in η is chosen so that its real component is positive.)

It is important to note that in order to obtain this relatively simple analytical description for x-ray reflectivity, it was necessary to assume that the fractional amplitude that is absorbed within a unit cell layer, σ, is small as compared with unity. It can be easily shown[5] that this condition is fulfilled when d is sufficiently small that the angle for the first order reflection, θ_1, is greater than about three times the critical angle for total reflection from the analyzer, θ_c. ($\sigma = (\pi/2)(\theta_c/\sin \theta_1)^2$) This is usually not a serious limitation because for nearly all practical applications in spectroscopic analysis, $\theta_1 \gg \theta_c$.

A more rigorous solution for the reflectivity of a multilayer consisting of N layer pairs of a heavy and light element (e.g. a sputtered tungsten-carbon multilayer) may be obtained by consecutively applying the E&M Fresnel reflection equation at each of the 2N interfaces, using as the material constants the refractive indices, $n(= 1 - \delta - i\beta)$ descriptive of each elementary layer, where:

$$\delta = \frac{r_o \lambda^2}{2\pi} nf_1 \qquad (8)$$

$$\beta = \frac{r_o \lambda^2}{2\pi} nf_2 \qquad (9)$$

Here n is the no. density and f_1 and f_2 are the atomic scattering factor components for the element (or compound) comprising each sub-layer. In Fig. 9 we have plotted the total reflection region and the first three orders of reflection for a tungsten-carbon multilayer ($N = 30$, $2d = 70$ A and with the tungsten layer of 0.4 d thickness) comparing the optical E&M model[6] (OEM) (dashed line) and our modified Darwin-Prins model (MDP). As may be noted, the results are essentially identical.
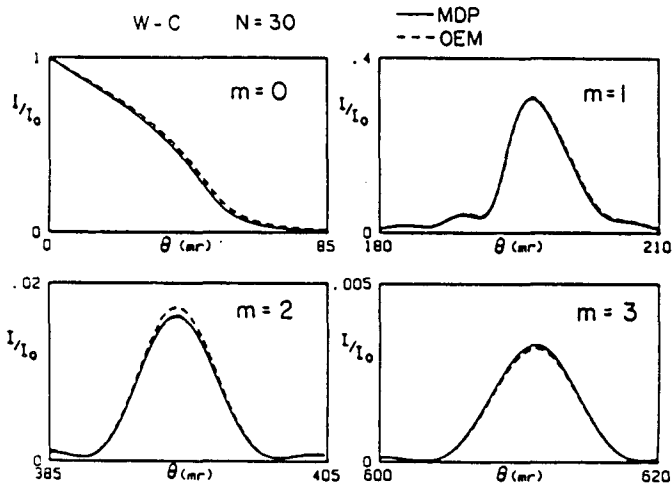

Fig. 9. Comparing the optical E&M (dashed line) and the MDP calculated spectra for a tungsten-carbon multilayer with 30 layers of the same photon energy as in Fig. 7.

It was noted above that in order to calculate the crystal/multilayer reflectivity characteristics using the MDP model, we only need to specify the unit cell volume, V, and its complex structure factor, F ($= F_1 + iF_2$). The total scattering factor per unit cell, F_0 ($= F_{01} + iF_{02}$) is set equal to F with $\theta = 0$. For the crystallographic case in which the unit cell is comprised of a collection of n_p atoms of

type P, of atomic scattering factor f_p ($= f_{p1} + if_{p2}$), and located at position z_p from a plane of symmetry of the unit cell (z_p is perpendicular to the reflecting planes), the structure factor components are given by the relations:

$$F_1 = \sum_p x_p f_{p1} \cos(\frac{4\pi z_p \sin\theta'}{\lambda'}) \qquad (10)$$

$$F_2 = \sum_p x_p f_{p2} \cos(\frac{4\pi z_p \sin\theta'}{\lambda'}) \qquad (11)$$
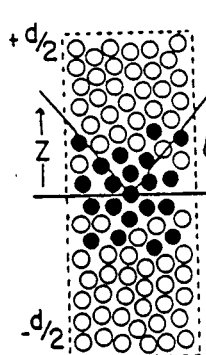
In the case of a continuous high density distribution of two elements (or compounds) for the sputtered/evaporated multilayers, the structure factors are given as noted in Fig. 10 by:

$$F_1 = \frac{V}{d} \int_{-d/2}^{d/2} (nf_1 + n'f_1')\cos(\frac{4\pi z}{\lambda'}\sin\theta')dz \qquad (12)$$

$$F_2 = \frac{V}{d} \int_{-d/2}^{d/2} (nf_2 + n'f_2')\cos(\frac{4\pi z}{\lambda'}\sin\theta')dz \qquad (13)$$

Here n and n' are the no. densities of the two elements at position z within the assumed symmetric unit cell and m is the number of unit cells per unit area and is equal to (d/V), where V is the volume of the unit cell.

(DENSELY PACKED)

$$mF_1 = \int_{-d/2}^{d/2} (nf_1 + n'f_1')\cos(\frac{4\pi z}{\lambda}\sin\theta)dz$$

$$mF_2 = \int_{-d/2}^{d/2} (nf_2 + n'f_2')\cos(\frac{4\pi z}{\lambda}\sin\theta)dz$$

n,n' = No. Densities of Heavy, Light Atoms at Position z

m = No. of Unit Cells Per Unit Area

Fig. 10. Defining the structure factor components for the unit cell of a sputtered/evaporated multilayer. Model density distributions that are considered include sharp interface, a compound transition layer, a linearly varying density of each element through a transition layer and interface roughness.

Our MDP model predicts a refraction modified angle, θ', and wavelength, λ' within the crystal/multilayer, consistent with Snell's Law, and correspondingly it predicts a shift in the diffraction peak position from that angle given by the Bragg relation, $m\lambda = 2d \sin \theta_0$ by an amount given by $\delta/(\sin \theta_0 \cos \theta_0)$. The refractive index decrement, $\delta = r_0\lambda^2 F_{01}/2\pi V$ is explicitly independent of the structure factor, F, while the intensity of the diffracted line is strongly dependent upon the structure factor, $F_1 + iF_2$, as defined in (10) through (13) in terms of the angle, θ', and wavelength, λ', presented to each unit cell within the crystal/multilayer. It can be readily shown that the sin θ'/λ' quantity in the structure factor relations can be expressed in the desired θ and λ variables by the relation:

$$\sin \theta'/\lambda' \approx (\sin\theta/\lambda)\sqrt{1 - \frac{2\delta}{\sin^2\theta}} \qquad (14)$$

(Note: This correction only applies for the calculation of the large angle Bragg diffractions for $m \geq 1$ and not for the "total reflection" region ($m = 0$).)

In Fig. 11 and in Table 1 we present a series of calculated integrated reflectivity curves, R vs E(eV), over the energy range 100-10 000 eV for those crystal/multilayer systems that are amenable to bending to the elliptical curvatures required for the spectrograph
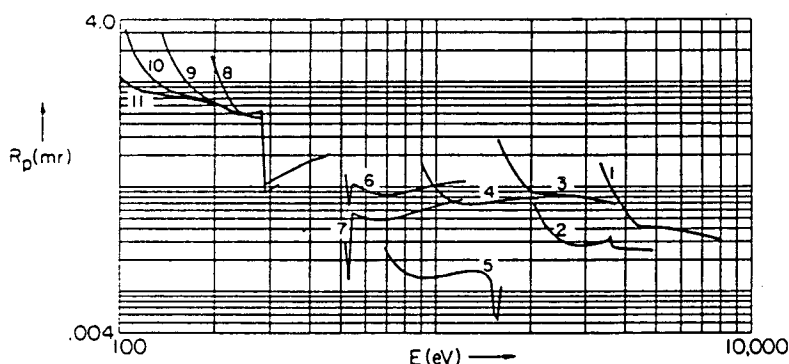

Fig. 11. Integrated reflectivity, R(mrad), vs photon energy, E(eV), for eleven crystal/multilayers that may be applied to cover the 100-10 000 eV region as elliptical analyzers and as listed in Table 1. The R plots have been calculated using the MDP model.

Table 1. Crystal/multilayers having integrated reflectivities as plotted in Fig. 11

No.	Crystal name	Indices (hkl)	2D	Diffraction order	E (eV) limits $22.5°\text{-}(\theta) - 67.5°$	R (45°)[b] (mrad)
1	LiF	(200)	4.03	1	8046—3333	0.0433
2	Mica	(002)	19.84	3	4900—2029	0.0286
3	PET	(002)	8.74	1	3707—1535	0.0907
4	Gypsum	(020)	15.19	1	2134— 884	0.0711
5	Mica	(002)	19.84	1	1633— 676	0.0136
6	RAP	(10$\bar{1}$0)	26.12	1	1240— 514	0.0848
7	KAP	(10$\bar{1}$0)	26.63	1	1217— 504	0.0488
8	Laurate[a]		70.00	1	463— 192	0.4878
9	Stearate		100.00	1	324— 134	0.8262
10	Lignocerate		130.00	1	249— 103	0.9373
11	Melissate		160.00	1	203— 84	0.8974

[a] Molecular multilayers of lead salts of straight-chain fatty acids.
[b] For Bragg angle, θ, equal to 45°.

described in the Introduction.   In Fig. 12 we compare the calculated and
the experimental integrated reflectivity values for the potassium acid
phthallate analyzer (KAP) using both the Darwin-Prins and the mosaic
models.[5]   Illustrated here is a measured sharp reflectivity "spike" at
the oxygen-K absorption edge resulting from a condensed-matter molecular
orbital resonance: a reminder that the atomic scattering description
used here can apply only outside the absorption edge threshold regions
where scattering may be considered "atomic-like" and unaffected by the
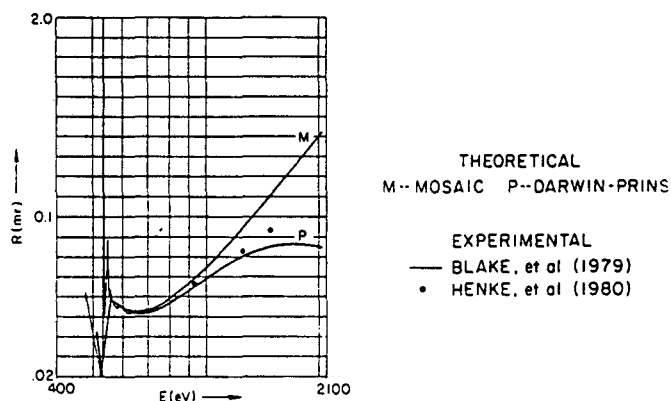chemical or solid state.

THEORETICAL
M-·MOSAIC   P--DARWIN-PRINS

EXPERIMENTAL
—— BLAKE. et al (1979)
• HENKE. et al (1980)

Fig. 12. The integrated reflectivity curves for the potas-
sium acid phthalate (KAP) crystal calculated using the MDP
and the Mosaic crystal models and compared with experimental
measurement.   These models, using the atomic scattering
factors, cannot be applied near absorption thresholds where
chemical and/or solid state effects may occur--e.g. the
sharp, reflectivity "spike" appearing here near the Oxygen-K
edge at 530 eV.

Finally, in Figs. 13 and 14, we present a comparison of the
experimental and MDP model characterizations of two synthesized large
d-spacing multilayers, a Langmuir-Blodgett lead stearate and a sputtered
tungsten-carbon.[4] For our modeling of the W-C analyzer we assumed a
linearly varying density in the tungsten-carbon transition layer (or
equivalently, an interface roughness layer[5]).

Fig. 13. The Langmuir-Blodgett Lead Stearate Multilayer -
2d - 99 A, N - 100. Comparison of the MDP model curves with
experimental values for integrated reflectivity, R, peak
efficiency, P, FWHM, ω, and resolving power, E/ΔE.

Characterization of a Molecular Lead Stearate Multilayer

14
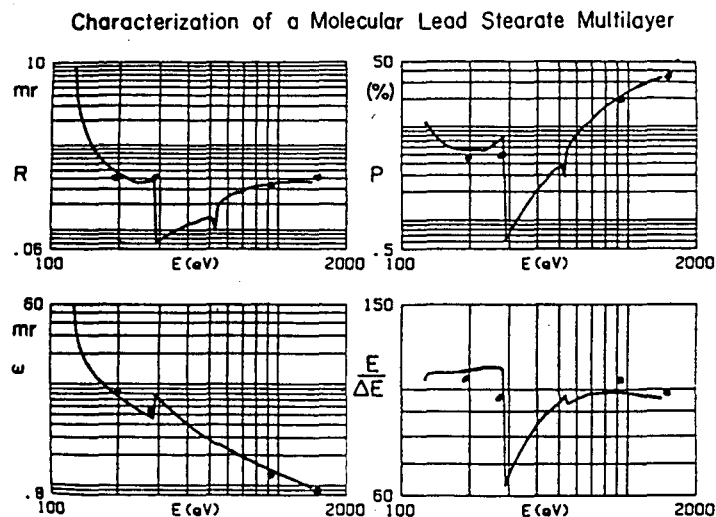
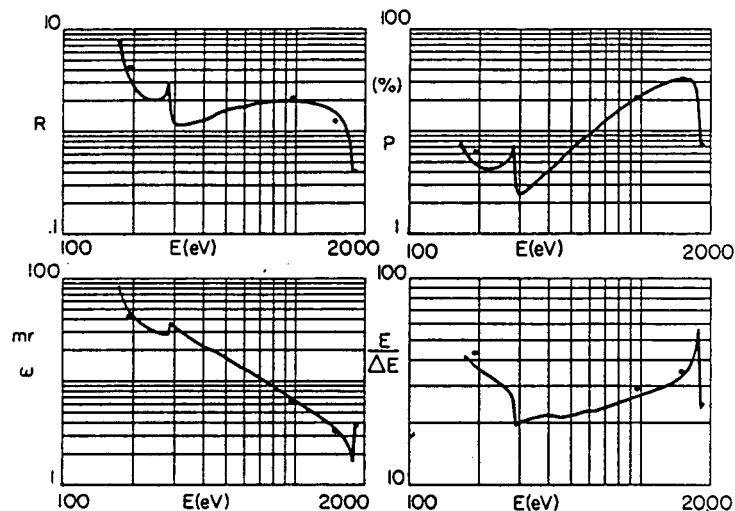## Characterization of a Sputtered Tungsten-Carbon Multilayer

Fig. 14. The sputtered Tungsten-Carbon Multilayer. 2d = 75 A, N = 120. Model fit for 25 A tungsten and 17 A tungsten-carbon interface with an assumed linear variation of densities in the interface region. Comparison of MDP model curves with experimental values for integrated reflectivity, R, peak efficiency, P, FWHM, ω, and resolving power, E/ΔE.

Fig. 15 illustrates the complementary aspect of the sputtered/evaporated and the molecular Langmuir Blodgett analyzers. For the same d-spacing and for appropriate composition these analyzers have similar peak reflectivities, but the high-density sputtered/evaporated multilayer has the higher integrated reflectivity and correspondingly, lower resolving power.
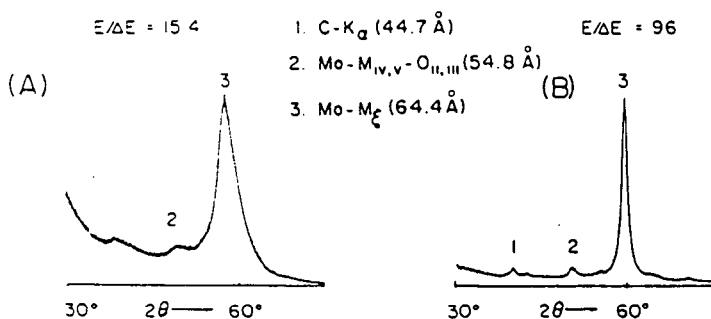

Fig. 15. Comparing spectra measured with the flat analyzers, (A) sputtered tungsten-carbon of 2d = 132 A and (B) Langmuir-Blodgett, lead lignocerate of 2d = 129 A. As suggested here by optimized measurements with sputtered and molecular multilayers of about the same 2d values, peak reflectivities are similar but the high density sputtered multilayers have appreciably higher integrated reflectivities and correspondingly lower resolving powers.

B. Mirrors and Filters

For optimized absolute x-ray spectrometry it is important to suppress the low and high energy background which may be particularly intense in the new large synchrotron and plasma sources. This "extra" radiation can thermally distort the analyzer and can appear in the measured spectrum as high-order diffracted or diffuse scattered background. As noted earlier, a primary monochromator combining the high-energy cut-off characteristic of a small-angle reflection and the low-energy cut-off characteristic of an absorption edge filter can provide an effective suppression of this "extra" radiation. The band-pass characteristic of a practical mirror-filter monochromator is presented in Fig. 16 for a 30 mrad reflection from an aluminized mirror and for transmission through a 300 μg/cm^2 copper foil.

The filter transmission, F, is readily calculated using the energy dependent mass absorption coefficient, μ, and the mass per unit area thickness, m, of the filter material, with the usual relation:
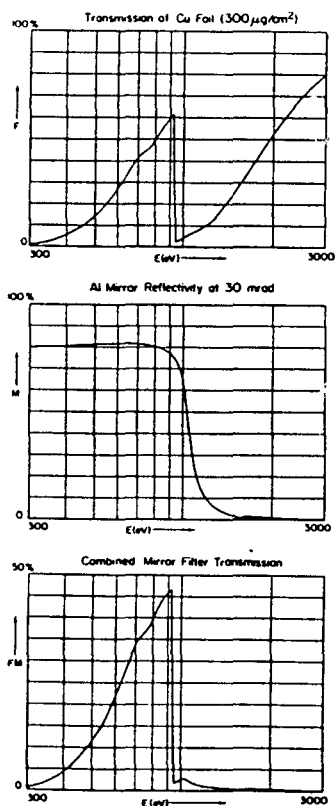
$$F = \exp(-\mu m) \qquad (15)$$

Fig. 16. The band-pass characteristic of the mirror-filter combination of a 30 mrad reflection from Aluminum and transmission through a 300 μm/cm^2 Copper foil.

It can be shown[5] that the Darwin-Prins relation for the semi-infinite crystal can accurately represent the Fresnel small-angle reflection characteristic, M, by setting the order parameter, m, in the variable, z, equal to zero. For the homogeneous mirror, the unit cell is simply described by a uniform distribution of a single element (or compound). Alternatively, the two intensity polarization components can be expressed by the following Fresnel relations for the relative intensities[7]:

For the incident E-vector perpendicular to the reflection plane,

$$I_o(\theta) = \frac{4\rho^2(\sin\theta - \rho)^2 + \gamma^2}{4\rho^2(\sin\theta + \rho)^2 + \gamma^2}.$$ (16)

and for the polarization ratio,

$$\frac{I_\pi(\theta)}{I_o(\theta)} = \frac{4\rho^2(\rho - \cos\theta\cot\theta)^2 + \gamma^2}{4\rho^2(\rho + \cos\theta\cot\theta) + \gamma^2},$$ (17)

where the parameter, ρ, is given by:

$$\rho = (1/2)\{\sin^2\theta - \alpha + [(\sin^2\theta - \alpha)^2 + \gamma^2]^{1/2}\}.$$ (18)

and $\alpha = 2\delta$ and $\gamma = 2\beta$
The optical constants, δ and β, are given in terms of the total scattering factor per unit volume, nF, by (8) and (9). (Again, these model calculations, using the atomic scattering factors, can be accurately applied only for photon energies outside the absorption threshold regions.)

Presented in Fig. 17 are comparisons of the Fresnel model prediction and the experimental measurement of the mirror reflectivity, M, for high quality surfaces of beryllium, aluminum and fused quartz[8] measured by the procedure outlined above (see Fig. 6).
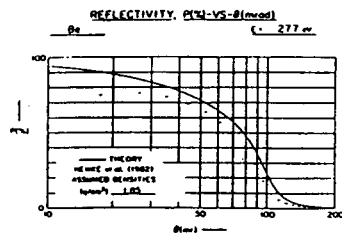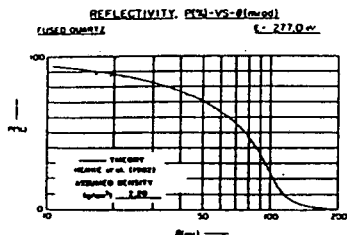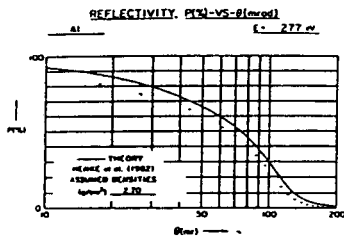
REFLECTIVITY, P(%)-VS-θ(mrad)

Fig. 17. Comparing Fresnel small-angle reflection curves with experimental measurement from high quality mirror surfaces of Beryllium, Aluminum and Fused Quartz.

C.   Photographic Films

Described in Fig. 18 is our method for measuring the optical density, D, vs absolute exposure, I, response of a photographic film. A characteristic line spectrum from a filtered x-ray source is scanned along the detection circle of an elliptical analyzer by a proportional counter to yield the absolute peak intensity for each line in photons per μm^2-sec. Then a photographic camera is introduced with its 35 mm film transported along the same detection circle, and a series of exposures are taken at known exposure times. The film is processed by a controlled, standard procedure and microdensitometered spectra are obtained, as shown in Fig. 18. The slits on the proportional counter and on the microdensitometer are matched, and have widths that are small compared to the instrument-broadened diffraction lines. Plots of density, D, vs Exposure, I(photons/μm^2) for corresponding peaks yield the D-I calibration curves shown in Fig. 19 for recently collected data on the high energy x-ray films, Kodak SB-392 (single emulsion) and DEF (double emulsion). This procedure is operationally identical, but the reverse of that which is used to determine an absolute exposure from a measured density.

PROPORTIONAL COUNTER SCAN OF Cu-L SPECTRUM

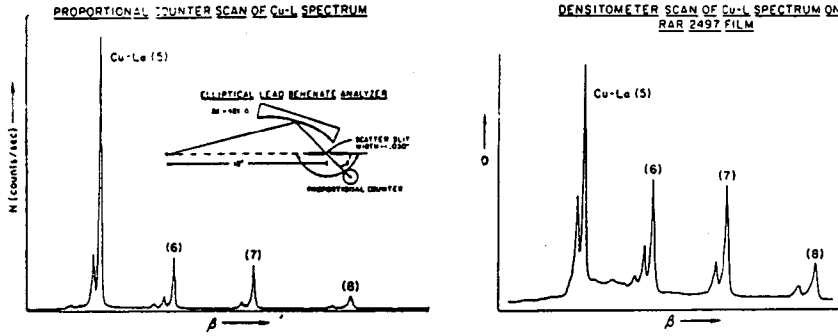DENSITOMETER SCAN OF Cu-L SPECTRUM ON RAR 2497 FILM

Fig. 18. Illustrating the method for photographic film calibration. An elliptical analyzer is used to place spectra of the desired photon energies along a detection circle. The absolute intensity spectrum is determined with a gas flow proportional counter with pulse height discrimination and a series of photographic exposures are then made. The photographic spectra are microdensitometered with a slit which matches that of the proportional counter and of width that is small as compared with that of the instrument-broadened diffraction lines. At corresponding line peaks, specular density values, D, are compared with absolute exposure values I(photons/μm^2) to yield the D-I calibration curves. This calibration procedure is operationally similar to that used (in reverse) for the determination of absolute exposures from microdensitometered spectra.

SB 392 Density vs Exposure

x Henke et al (1986).
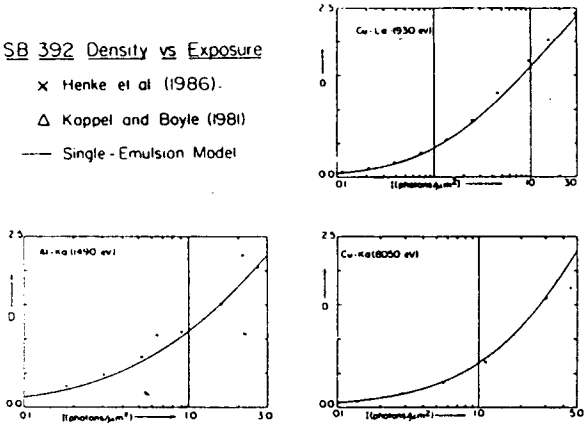
△ Koppel and Boyle (1981)

—— Single-Emulsion Model

Fig. 19. Examples of Specular Density, D vs Exposure, I(photons/μm^2) curves for Kodak's single emulsion SB-392 and double-emulsion DEF x-ray films. These experimental data are compared with the predictions of our energy- dependent model response equations (21) and (22).

DEF Density vs Exposure

o Henke et al. (1986)

x Rockett et al. (1985)

+ Phillips and Phillips (1985)

— Double Emulsion Model
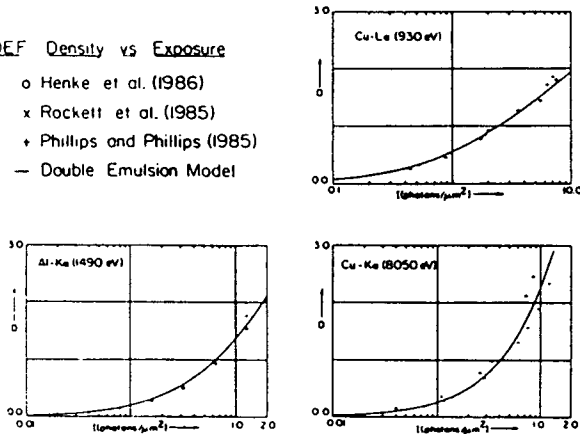
The smooth curves shown in Fig. 19 which fit the experimental data are D-I curves obtained from our analytical photographic film response model relations. The model relations are functions of the exposure, I(photons/μm^2), photon energy, E(eV) and the angle of incidence, θ, and require only two fitting parameters, a and b.[9,10,11]

The general model description is shown in Fig. 20. The x radiation that reaches a layer of silver bromide grains at depth x (distributed within gelatin) is equal to that incident at angle θ, less the fraction absorbed by the protective supercoat and by the heterogeneous grain-gelatin emulsion above the layer. It follows that the probability for a photon absorption within a AgBr grain can be expressed as a function of the geometric grain cross section, σ, the grain diameter, d, the supercoat thickness, t, and the energy-dependent linear absorption coefficients, μ_1, μ_0 and μ', for AgBr, gelatin and the heterogeneous emulsion, respectively. It is further assumed for the 100-10 000 eV region of interest here that (1) the photon energies are sufficiently high that only one photon is required to render a grain developable and (2) that these energies are sufficiently low that the photoelectrons generated in the gelatin do not have sufficient range or energy to render additional unexposed grains developable. We list here the "universal" model relations that have been derived from such general model assumptions:[9,10,11]

For a monolayer of AgBr grains with no supercoat (designed for EUV and low energy x-rays as the Kodak 101):

$$D = a_1[1 - \exp(-b_1\beta_1 I)] \qquad (19)$$

For a thick emulsion (totally absorbing):

$$\alpha D = a \ln(1 + b\beta I). \qquad (20)$$

PROBABILITY FOR ABSORPTION WITHIN AgBr GRAIN AT DEPTH, x
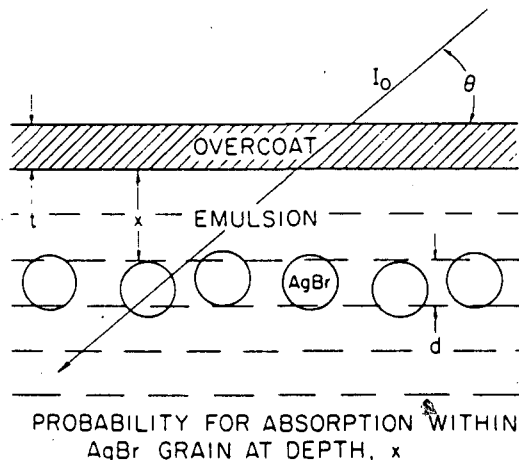
$$\sigma I \left[1 - \exp(-\mu_1 d) \right] \exp\left[\frac{-(\mu_0 t + \mu' x)}{\sin \theta} \right]$$

Fig. 20. The probability for a photon absorption within a AgBr grain of cross section, σ, at depth x within the emulsion and given here is a function of the grain diameter, d, the supercoat thickness, t, and the energy-dependent linear absorption coefficients, μ_0 of the supercoat, μ_1 of AgBr and μ' of the heterogeneous emulsion--for an exposure, I(photons per unit area) from direction, θ. Other model assumptions are (1) for the 100-10 000 eV photon energy region of interest here, only one photon absorption is required to render a grain developable and (2) the cross-section, σ, is independent of the photon energy.

For a thin partially absorbing emulsion of thickness T:

$$D = \qquad \alpha D = a \ln \frac{1 + b\beta I}{1 + b\beta I \, \exp(-\mu' T/\sin \theta)} \cdot \qquad (21)$$

And, finally, for a double-emulsion film on a plastic base of thickness, t_b and linear absorption coefficient, μ_b:

$$\alpha D = a \ln \left(\left[\frac{1+b\beta I}{1+b\beta I \exp[(-\mu' T)/\sin\theta]} \right] \left(\frac{1+b\beta I \exp[(-\mu_b t_b - \mu' T)/\sin\theta]}{1+b\beta I \exp[(-\mu_b t_b - 2\mu' T)/\sin\theta]} \right) \right] \qquad (22)$$

In these expressions the factors; β_1, α and β yield the dependence upon photon energy, E(eV) and the angle of incidence, θ, and are given in Refs. 9, 10 and 11.

Having determined the fitting parameters, a and b, by least squares fitting to D-I data at a few representative photon energies, the complete energy response may then be accurately predicted. These semi-empirical relations can then be used, for example, to derive the absolute film sensitivity curves as shown in Fig. 21. Here, sensitivity S is defined as the reciprocal of the exposure, I(photons/μm^2) which is required to produce a specular density, D, of 0.5.
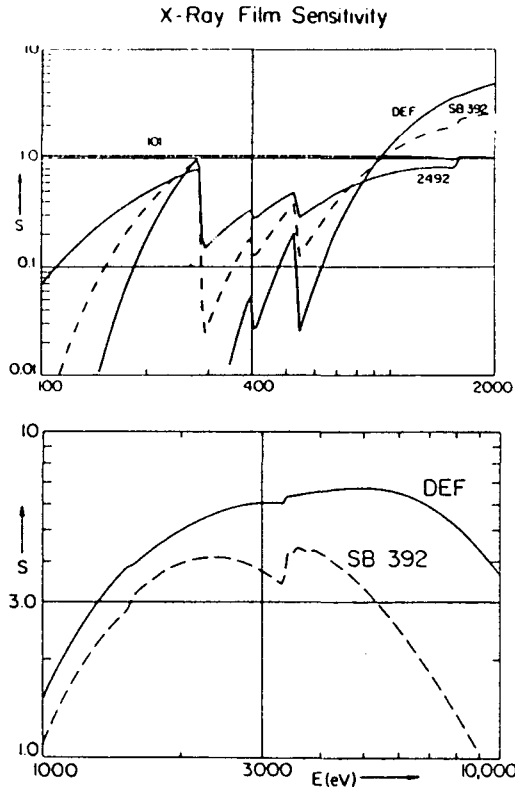

X-Ray Film Sensitivity

Fig. 21. Comparing the film sensitivities in the 100-10 000 eV region for the Kodak films. 101 (approximately a mono-layer of AgBr grains without supercoat). the single emulsion films, RAR 2492 and SB 392 and the double emulsion film DEF. Here sensitivity, S, is defined as the reciprocal of the exposure, I(photons/μm^2) required to generate a specular density of 0.5.
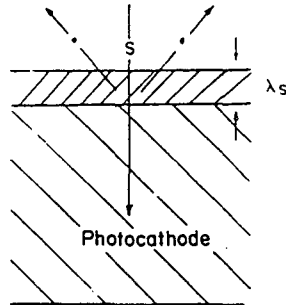
D. Photocathodes

The position sensitive photoelectric detectors that are applied in
x-ray spectroscopy include arrays of discrete x-ray diodes, x-ray streak
cameras (as described above) and the multichannel plate amplifier
detection systems, all of which utilize the basic photocathode element
to convert the x-ray photon intensity to an electronic current by
photoemission. The energy distribution of the emitted electrons from
either a front or back surface (transmission) photocathode is
illustrated in Fig. 22. Typically most of the electrons are emitted as
secondary electrons in the 0-10 eV region and only a few percent or less
escape elastically through the photocathode surface as the original
higher energy primary photoelectrons and Auger electrons. In the

Fig. 22. Describing the electron energy distribution that
is emitted from an x-ray photocathode. Only a small percen-
tage of the electrons are emitted as elastically escaping
high energy photoelectrons and Auger electrons. Most of the
electron emission is within a secondary electron distribu-
tion in the 0-10 eV region and measured by the photocath-
ode's characteristic quantum yield, Y (electrons/photon).
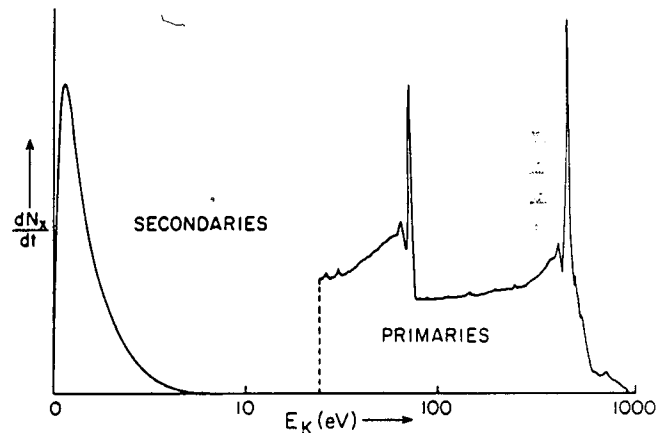
picosecond time-resolving detectors (e.g. the x-ray streak camera) the
primaries are rejected and the higher energy secondaries arrive at the
end of the streak camera sooner than the slower secondaries thereby
setting a limit on the time resolution. For example, for the relatively
sharp energy distribution width of about 1.5 eV characteristic of a CsI
photocathode, and for the accelerating fields within the typical streak
camera, an intrinsic time resolution of about two picoseconds may be
expected. The total number of electrons within this secondary electron
distribution is determined by the photocathode's quantum yield, Y, which
is the number of electrons emitted per normally incident photon for the
front surface photocathode. As suggested in Fig. 23 (for front surface
operation), the photoemission yield for x-rays is characteristically low
because most of the initial primary electrons and subsequently generated
secondary electrons are deposited deeply within the photocathode,
outside the escape depth region. The fraction of the incident intensity
that is photoabsorbed within this escape depth is given by the linear

$$Y_f \sim E\mu(E)\rho\lambda s$$

E - photon energy

$\mu(E)\rho$ - linear x-ray absorption coef.

λ_s - secondary electron escape depth

Fig. 23. The energy dependent x-ray photocathode quantum yield, Y, is proportional to the fraction of the normally incident photons that are absorbed within the escape depth region (i.e. to the linear absorption coefficeint, $\mu\rho$ times the escape depth, λ_s) and to the number of secondary electrons generated by a photon absorption (which is proportional to the photon energy, E, since the shape of the secondary electron energy distribution is independent of the photon energy).

absorption coefficient, $\mu\rho$ multiplied by the escape depth, λ_s. Because the shape of the secondary electron distribution is determined by the surface electronic state of the photocathode and does not depend upon the exciting photon's energy, E, it follows that the total number of emitted electrons should be proportional to E as well.[12] Therefore, in our modeling of the x-ray photocathode we establish the photon energy dependence of the quantum yield to be given by:

$$Y \sim E\mu(E)\rho\lambda_s \qquad (23)$$

In Ref. 12 we describe our method and instrumentation for the absolute measurement of photocathode quantum yields in the photon energy region of 100-10 000 eV. Examples of these measurements for the gold and cesium iodide photocathodes are presented here in Fig. 24. As can be seen by the superposition of $E\mu(E)$ curve on the plot of data, $E\mu(E)$ indeed follows the experimental photocathode energy dependence as suggested by (23). The considerably increased quantum yield of the cesium iodide photocathode (by a factor of about ten) is mostly the result of the larger escape depth λ_s which is determined by the longer mean free path of the secondary electrons within this insulator (electron-phonon interaction length) as compared to that for the metal photocathode (electron-electron interaction length).

III. X-RAY INTERACTION COEFFICIENTS

In Sec. II we have summarized our developments of efficient, analytic spectrographic response functions based upon the description of x-ray absorption, reflection and diffraction using the photon energy-dependent fundamental parameters, the atomic photoabsorption cross sections and the atomic scattering factors. We have demonstrated
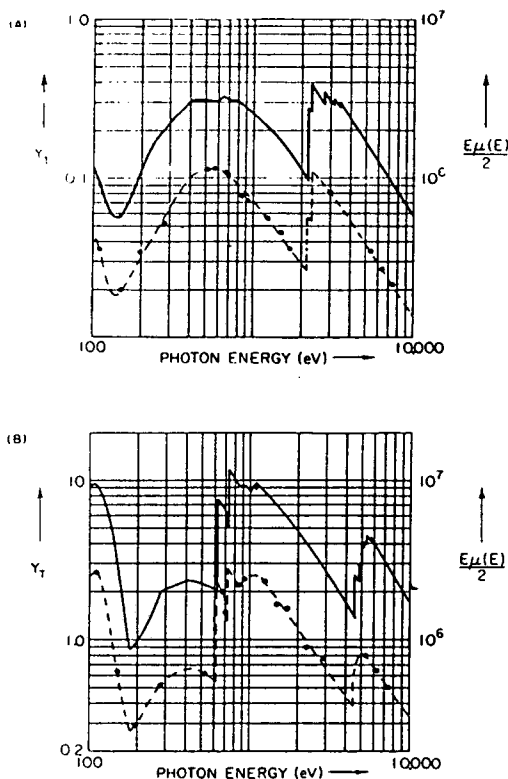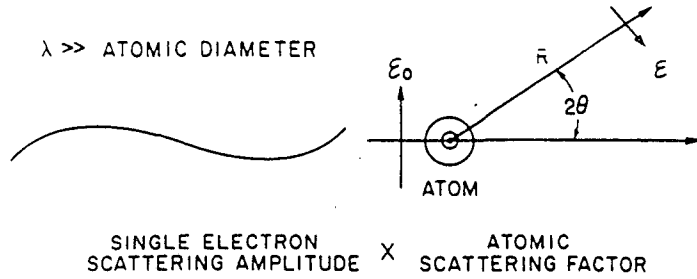
Fig. 24. Examples of measured photocathode front surface yield, Y (electrons/photon) vs photon energy, E(eV) for (A) a 300 A Au film and (B) a 3000 A cesium iodide film. The energy dependence expressed in Fig. 23 is demonstrated here by the superposition of the E μ(E) curves on these log-log plots. The considerably higher yields shown here for the CsI photocathode is predicted in our model by the fact that the escape depth for CsI (electron-phonon interaction length) is about ten times that of Au (electron-electron interaction length).

that our analytical modified Darwin-Prins (MDP) model for mirror and multilayer reflection is generally more efficient and yields results that are essentially identical to those obtained with the optical E&M model using the macroscopic material constants, δ and β. With either theoretical approach, the material properties can be derived from the atomic scattering factors for the photon energies outside the absorption threshold regions where the photon interactions within condensed matter may be considered to be with essentially free atoms. To facilitate accurate and detailed calculations of the model descriptions presented in Sec. II', we have established photoabsorption and atomic scattering factor tables for 94 elements within the 100-10 000 eV region.[13,14,15] A brief review of this work is presented here.

We define the atomic scattering factor, f ($= f_1 + if_2$) in Fig. 25 and have calculated the atomic scattering factors using the Kramers-Kronig dispersion relations based upon our compilations of experimental/theoretical photoabsorption cross sections. These relations are:

$$f_1 = Z + C \int_0^\infty \frac{\epsilon^2 \mu_a(\epsilon) d\epsilon}{E^2 - \epsilon^2} \tag{24}$$

$$f_2 = (1/2)\pi C E \mu_a(E), \tag{25}$$

λ >> ATOMIC DIAMETER

SINGLE ELECTRON   X   ATOMIC
SCATTERING AMPLITUDE   SCATTERING FACTOR

$$\mathcal{E}(\theta,\lambda) = -\left[\mathcal{E}_0\left(\frac{r_0}{R}\right)P(2\theta)\right](f_1(\lambda) + if_2(\lambda))$$

Fig. 25. Low-energy x-ray scattering by an atom. The amplitude scattered may be described by an atomic scattering factor, $f_1 + if_2$, multiplied by the amplitude that would be scattered by a single Thomsonian electron in the same x-radiation field. Here r_0 is the classical electron radius; R the radial distance to the point of measurement; and $P(2\theta)$ is the polarization factor that is equal to unity or cos 2θ, depending upon whether the incident electric vector (of magnitude $\mathcal{E}_0$) is perpendicular or parallel to the plane of scattering. For the low-energy x-ray region for which the wavelengths are large compared with the atomic dimensions, the scattering of each atomic electron at any angle is with the same phase as for the forward direction. The atomic scattering factor is thus independent of the angle of scattering, 2θ.

where E is the photon energy, $C \doteq (\pi r_0 hc)^{-1}$, r_0 is the classical electron radius, h is Planck's constant, and c is the speed of light. The atomic absorption cross section, μ_a, is related to the mass absorption coefficient $\mu(cm^2/gm)$, by:

$$\mu_a = A\mu/N_0 \qquad\qquad (26)$$

where A is the atomic weight and N_0 is Avogadro's Number. In our numerical integrations for the values of f_1 in (24) it was considered sufficient to take the integration range on ϵ from 30 eV to 85 keV, using "state of the art" values for $\mu(E)$ to obtain the required μ_a values.

For the higher photon energies where the wavelength becomes comparable to the dimensions of the atom, the individual atomic electrons may not be scattering in phase, and the atomic scattering factor will be reduced by the effect of the interference of these electronic scattering components. For the forward scattering case (e.g. in small angle reflection), and within the entire 100-10 000 eV region of interest here, all atomic electrons are scattering essentially in phase and the atomic scattering factor, f_1, given by (24) needs no correction. However, it can be shown that for the larger angles of scattering the value of f_1 given by (24) should be corrected by replacing the atomic number, Z, by the angle-dependent form factor, f_0, for the given atom. (In Ref. 14 we list the sources for the tabulated form factors for all elements and various charge states.) Thus the atomic scattering factor for the larger angles of scattering (e.g. for Bragg diffraction) may be more accurately given as:

$$f = f_1 - \Delta f + if_2 \qquad (27)$$

where

$$\Delta f = Z - f_0. \qquad (28)$$

In Fig. 26 we have plotted the modulus, $\sqrt{(f_1^2 + f_2^2)}$, of the atomic scattering factor for neon (Z = 10) calculated as describe. above for the two scttering angles, 0° and 180°. Also plotted here are modulus values based upon nearly exact S-Matrix theoretical calculations (via a very expensive computer program) by Pratt, et al. As shown in Fig. 26, for most practical purposes the relatively simple Kramers-Kronig model and the simple form factor correction given above are sufficiently accurate.

Fig. 26. Plots of the modulus of the atomic scattering factor, $\sqrt{f_1^2 + f_2^2}$, vs photon energy, E(eV) at 0° and 180° scattering angles for neon (Z - 10). Compared here are the atomic scattering factor modulus values calculated by the relatively simple Kramers-Kronig dispersion model and by the nearly exact (but expensive) 2nd order S-Matrix theoretical model. Also demonstrated here is the accuracy of the simple form factor correction that is applied in our calculation for large-angle scattering.
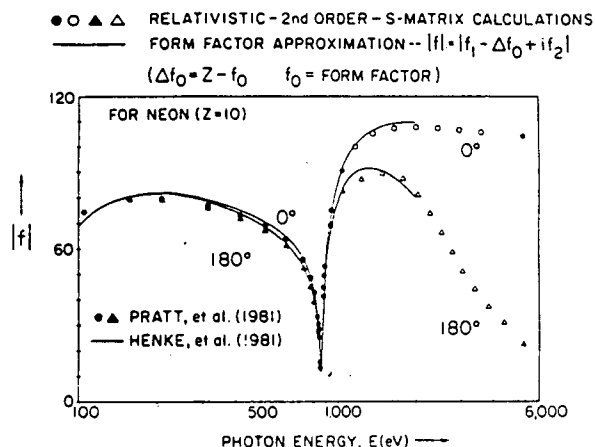
Finally, Fig. 27 (taken from our cross section tables[14]) presents plots of the atomic scattering factor components, f_1 and f_2, for Aluminum, illustrating in f_1 the strong anomolous dispersion throughout this photon energy region and in f_2 a comparison of our fit curve with data calculated directly from typical experimental measurements of μ using (25) and (26).
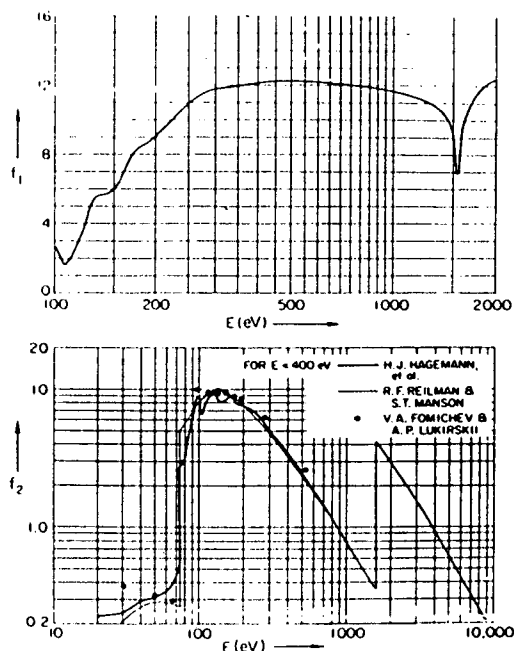

Fig. 27. Examples of plots of the atomic scattering factor components, f_1 and f_2 (for Aluminum) taken from Ref. 14. Illustrated here, in f_1, is the strong anomolous dispersion through this photon energy region, and in f_2, a comparison of our fit curve with present experimental photoabsorption data applying relations (25) and (26).

ACKNOWLEDGEMENTS

BIBLIOGRAPHY

1. B.L. Henke and P.A. Jaanimagi, "A Two-Channel, Elliptical Analyzer Spectrograph for Absolute Time-Resolving/Time-Integrating Spectrometry of Pulsed X-Ray Sources in the 100-10,000 eV Region," Rev. Sci. Instrum. 56, 1537-1552, 1985.

2. P.A. Jaanimagi and B.L. Henke, "An Absolutely Calibrated Time-Resolving X-Ray Spectrometer," Proc. of Soc. of Photo-Opt. Instrum. Engin. (SPIE), San Diego, 1985.

3. B.L. Henke H. T. Yamada and T. J. Tanaka, "Pulsed Plasma Source Spectrometry in the 80-8000 eV X-Ray Region," Rev. Sci. Instrum. 54, 1311-1330, 1983.

4. B.L. Henke, J.Y. Uejio, H.T. Yamada, and R.E. Tackaberry, "The Characterization of Multilayer Analyzers - Models and Measurements," in press, Opt. Engin. (August 1986).

5. B.L. Henke, H.T. Yamada and J.Y. Uejio, "Reflectivity Characteristics of Multilayers and Crystal Analyzers for the 100-10,000 eV Region - Theory and Experiment" (in preparation).

6. H.T. Yamada and T.J. Tanaka, "A Computer Program for the Calculation of the X-Ray Reflectivity Characteristics of Sputtered or Evaporated Multilayers Using the Optical E&M Model," LBL-21909, 1986.

7. B.L. Henke, "Ultrasoft X-Ray Reflection, Refraction and Production of Photo-electrons (100-1000 eV Region)," Phys. Rev. A6, 94-104, 1972.

8. B.L. Henke, J. Kerner and D. Kania, "Reflectivity Characteristics of Low-Energy X-Ray Mirror Monochromators" (in preparation).

9. B.L. Henke, S. L. Kwock, J. Y. Uejio, H. T. Yamada and G. C. Young, "Low-Energy X-Ray Response of Photographic Films: Part I. Mathematical Models," J. Opt. Soc. Am. 1, 828-849, 1984.

10. B.L. Henke, F. G. Fujiwara, M. A. Tester, C. H. Dittmore and M. A. Palmer, "Low-Energy X-Ray Response of Photographic Films: Part II. Experimental Characterization," J. Opt. Soc. Am. 1, 818-827, 1984.

11. B.L. Henke, J.Y. Uejio, G.F. Stone, C.H. Dittmore, F.G. Fujiwara, "High Energy X-Ray Response of Photographic Films. Models and Measurements", (in press, J. Opt. Soc. 1, October 1986).

12. B.L.Henke, J. P. Knauer and K. Premaratne, "The Characterization of
    X-Ray Photocathodes in the 0.1-10 keV Photon Energy Region,"
    J. Appl. Phys. 52, 1509-1520, 1981.

13. B.L. Henke, "Low Energy X-Ray Interactions: Photoionization,
    Scattering, Specular and Bragg Reflection," AIP Conf. Proc. 75,
    D. T. Attwood and B. L. Henke, Editors (Am. Instit. of Phys.,
    New York), 146-155, 1981.

14. B.L. Henke, P. Lee, T.J. Tanaka, R.L. Shimabukuro, and B.K.
    Fujikawa, "Low Energy X-Ray Interaction Coefficients:
    Photoabsorption, Scattering and Reflection. E = 100-2000 eV,
    Z = 1-94," At. Data Nucl. Data Tables 27, 1-144, 1982.

15. B.L. Henke, H.T. Yamada and J.Y. Uejio, "Fine-Spaced Photoabsorption
    Cross-Sections and Atomic Scattering Factors for the 94 Elements
    in the 100-10,000 eV Photon Energy Region" (in preparation as 8"
    floppy disk, RT-11 format).

LAWRENCE BERKELEY LABORATORY
TECHNICAL INFORMATION DEPARTMENT
UNIVERSITY OF CALIFORNIA
BERKELEY, CALIFORNIA 94720